Maus, S., Rother, M., Hemant, K., Stolle, C., Lühr, H., Kuvshinov, A., Olsen, N. (2006): Earth's lithospheric magnetic field determined to spherical harmonic degree 90 from CHAMP satellite measurements. - Geophysical Journal International, 164, 2, pp. 319—330.

DOI: http://doi.org/10.1111/j.1365-246X.2005.02833.x

Geophys. J. Int. (2006) **164,** 319–330 doi: 10.1111/j.1365-246X.2005.02833.x

Earth's lithospheric magnetic field determined to spherical harmonic degree 90 from CHAMP satellite measurements

S. Maus,[1,*,†] M. Rother,[1] K. Hemant,[1] C. Stolle,[1] H. Lühr,[1] A. Kuvshinov[2] and N. Olsen[2]

[1] *GeoForschungszentrum Potsdam, Telegrafenberg,* 14473 *Potsdam, Germany*
[2] *Danish National Space Center, Juliane Maries Vej 30,* 2100 *Copenhagen, Denmark*

Accepted 2005 October 7. Received 2005 August 10; in original form 2004 April 8

SUMMARY

The CHAMP magnetic field mission is providing highly reliable measurements from which the global lithospheric magnetic field can be determined in unprecedented resolution and accuracy. Using almost 5 yr of data, we derive our fourth generation lithospheric field model termed MF4, which is expanded to spherical harmonic degree and order 90. After subtracting from the full magnetic field observations predicted fields from an internal field model up to degree 15, an external field model up to degree two, and the predicted magnetic field signatures for the eight dominant ocean tidal constituents, we fit and remove remaining external fields and polar electrojet signatures in a track-by-track scheme. From a subset of least disturbed tracks, we estimate the MF4 model by least squares, damping ill-determined coefficients by regularization. The resulting MF4 model provides a good representation of the lithospheric field down to an altitude of about 50 km at lower latitudes, with reduced accuracy in the polar regions. Crustal features come out significantly sharper than in previous models. In particular, bands of magnetic anomalies along subduction zones become visible by satellite for the first time.

Key words: crustal field, crustal magnetization, field modelling, geomagnetic field, lithospheric field.

1 INTRODUCTION

Magnetic minerals in the crust (and possibly also in the upper mantle) give rise to a magnetic field, which is strong enough to be mapped by low-orbiting satellites. Global maps of this lithospheric field were first compiled from POGO (1965–1971) magnetic total intensity (scalar) measurements (Cain & Sweeney 1973; Regan *et al.* 1975). After recognizing that the internal magnetic field is not well constrained by scalar-only data (Backus 1970), the Magsat satellite (1979–1980) was equipped with a vector magnetometer and a star imager for accurate attitude determination, in addition to an absolute scalar magnetometer. Sometimes combined with the earlier POGO data, Magsat scalar and vector data was used in a number of different lithospheric field models (e.g. Cain *et al.* 1989; Cohen & Achache 1990; Arkani-Hamed *et al.* 1994; Ravat *et al.* 1995). However, due to the short duration of the Magsat mission, its eccentric dawn/dusk orbit and its attitude uncertainty, models prepared by different workers using different data sets, selection criteria and processing schemes disagreed significantly, particularly over areas of weak magnetization and over the polar regions. A comprehensive overview of these earlier satellite lithospheric magnetic field models and their interpretation is given by Langel & Hinze (1998).

20 yr on, the CHAMP satellite (launched 2000 July) is measuring the field in a low altitude, circular orbit with unprecedented accuracy (Reigber *et al.* 2002). Presently, two lines of lithospheric field models are being produced, which incorporate the new CHAMP data. One is the Comprehensive Model (Sabaka *et al.* 2004), which includes geomagnetic field parameters accounting for sources from the core to the magnetosphere. These parameters are estimated in a joint inversion. The Comprehensive Model contains the lithospheric field as one of many contributions. Since its input data presently includes noisy day time data to resolve the Sq current system, the present version, CM4, does not resolve small-scale lithospheric field structure very well and it is, therefore, limited to spherical harmonic (SH) degree 65.

In contrast, the MF series of field models is strictly focused on the lithospheric field. Our initial lithospheric field model MF1 (Maus *et al.* 2002) was only determined from the scalar (total intensity) data, acquired during the first year of the CHAMP mission. This model, and its revisions MF2 and MF3, which made use of CHAMP vector data, are available at http://www.gfz-potsdam.de/pb2/pb23/SatMag/model.html. Our fourth generation lithospheric field model MF4 is based on further improvements in

*Now at: the Cooperative Institute for Research in Environmental Sciences at the University of Colorado and NOAA's National Geophysical Data Center, USA.
†National Geophysical Data Center, NOAA E/GC1, 325 Broadway, Boulder, CO 80305-3328, USA. E-mail: Stefan.Maus@noaa.gov.

the processing methodology, including an improved correction for the effects of polar electrojets (PEJs). Here, we describe the processing scheme used to derive the MF4 model from almost 5 yr of CHAMP scalar and vector data.

Before estimating a lithospheric field model, it is worth while to consider some of the intended applications:

(1) It is necessary to subtract a lithospheric field model from satellite magnetic measurements in order to study other phenomena, such as ionospheric currents (Ritter *et al.* 2004a), pulsations (Sutcliffe & Lühr 2003) and magnetic signals due to ocean flow (Tyler *et al.* 2003). Due to the almost static nature of the lithospheric field, this correction can be retroactively applied to data from previous satellites, as well.

(2) The model can directly be used in geological and geophysical interpretation (Hemant *et al.* 2005; Fox Maule *et al.* 2005).

(3) It provides the long-wavelength lithospheric field for large-scale marine and aeromagnetic compilations and may fill in the unsurveyed areas for the World Digital Magnetic Anomaly Map (WDMAM) project.

The difference between these applications is that for the first case the model has to be accurate at satellite altitude. For the second case, one may wish to evaluate the field at a lower altitude to enhance smaller-scale features for geological interpretation. Finally, for the third and most challenging application, the model should ideally provide the lithospheric magnetic field at the Earth's surface. This may cause problems with the SH representation of the field, which is strictly valid only for shells larger than the equatorial radius of the Earth. In practice one, therefore, has to employ special downward continuation (e.g. Achache *et al.* 1987) or use a joint inversion (Ravat *et al.* 2002b) technique in order to evaluate the field close to the Earth's surface. In summary, from the point of view of these various applications, especially the high-degree coefficients (=small-scale features) of our new models have to be as accurate and noise free as possible in order to be suitable for the outlined purposes. This has been a guiding principle in deriving the MF series of models.

2 DATA SELECTION, PROCESSING APPROACH AND MODEL ESTIMATION

The input data were measured by the CHAMP satellite, which is orbiting the Earth at an inclination of 87.3°. From its initial altitude of 456 km it has decayed to 360 km after 5 yr, during which two orbital manoeuvres were carried out to increase the altitude and prolong the mission. The data utilized here are from the magnetometer package. Most important for this study are the readings of the absolute scalar Overhauser magnetometer (OVM). It samples the magnetic field magnitude at 1 Hz. Another instrument considered here is the triaxial fluxgate magnetometer (FGM). It delivers vector readings at a rate of 50 Hz. The data for this study are calibrated with respect to the scalar OVM and down-sampled to 1 Hz. A dual-head star camera system, mounted together with the magnetometer on an optical bench, provides the orientation of the measured field vectors with arc second precision. Vector data are only considered when readings from both camera heads are available. This provides a reduction in attitude noise. CHAMP scalar (OVM) and vector (FGM) data are available from 2000 August 8, 3 weeks after launch. The data basis for MF4, therefore, consists of almost 5 yr of scalar and vector data. The individual processing steps are summarized in the diagram of Fig. 1.

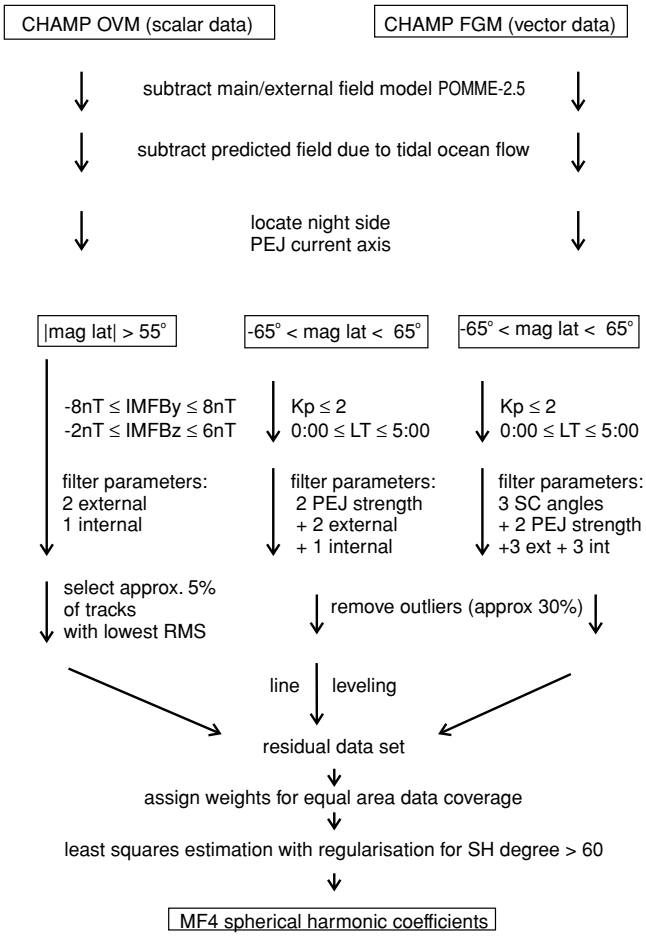

Figure 1. Processing scheme for deriving the MF4 model.

Table 1. Number of vector and scalar CHAMP measurements used in this study, where S.-polar tracks are below −55°, N.-polar are above 55°, and lower latitude tracks cover the overlapping range of −65° to 65° magnetic latitude.

	S.-polar	Low	N.-polar
Vector		907 000	
Scalar	675 543	2 519 365	714 723

They include subtracting models of the main and large-scale magnetospheric fields and a correction for tidal ocean fields. Remaining large-scale magnetospheric fields are removed by fitting a low-degree SH function to the data of each individual satellite track. Details of how the various field components are separated will be described in subsequent sections. Further corrections for ionospheric plasma effects, the magnetic signature of field-aligned currents and ocean induced fields by time-varying externals fields would be highly appropriate. However, at this time, such corrections are not yet available. Table 1 lists the final data numbers remaining after the following processing and selection steps.

2.1 Main field removal

The internal geomagnetic field is a superposition of the core field (main field), the lithospheric field, and fields induced by time-varying external sources. While the core field dominates at long

wavelengths, the shorter wavelengths are dominated by the lithospheric field. The transition occurs around degree 13–15. This transition is prominently manifested as a 'knee' in the geomagnetic power spectrum (see e.g. Backus *et al.* 1996). Below degree 13 the field is dominated by the core field, and above degree 15 by the lithospheric field. However, in areas of weak lithospheric fields, such as over young oceanic crust, the core field can dominate up to degree 15. If the smaller-scale internal field is displayed for degrees $\geq$15, as given by MF1, prominent stripes appear over the oceans, which are most likely part of the core field. These stripes largely disappear if the field is displayed for degrees $\geq$16. That is why MF2, MF3 and MF4 were chosen to start at degree 16 only. For the removal of the internal field up to degree 15, which also contains inseparable parts of the lithospheric field, we use the field model POMME-2.5 (Maus *et al.* 2005). The model includes the secular variation, secular acceleration and a new parametrization of external and induced fields, described in detail in Maus & Lühr (2005).

2.2 Tidal correction

The flow of conducting sea water through the Earth's magnetic field induces currents, which in turn give rise to secondary magnetic fields. For tidal flow, these signals reach amplitudes of 3 nT at 400 km altitude and are clearly identified in magnetic satellite data (Tyler *et al.* 2003). Since tidal ocean flow is well determined from satellite altimetry, a rather accurate prediction of its magnetic signal has been made (Kuvshinov & Olsen 2005) on a mesh with a spatial resolution of $1^\circ \times 1^\circ$, taking as input the depth integrated tidal flow velocity from the TPXO.6.1 global tidal model (Erofeeva & Egbert 2002), the shell conductance from the sea water using the global $5' \times 5'$ NGDC/NOAA's ETOPO bathymetry and the global sediment thickness given by the $1^\circ \times 1^\circ$ map of Laske & Masters (1997). Finally, for the underlying spherical conductor, the three-layer earth section of Schmucker (1985) was chosen. For details of the modelling, see Kuvshinov & Olsen (2005). Subtracting the predicted magnetic fields for the eight major tidal constituents almost completely removes the tidal signal from the magnetic residuals. The effect is illustrated in Fig. 2 for the Indian Ocean.

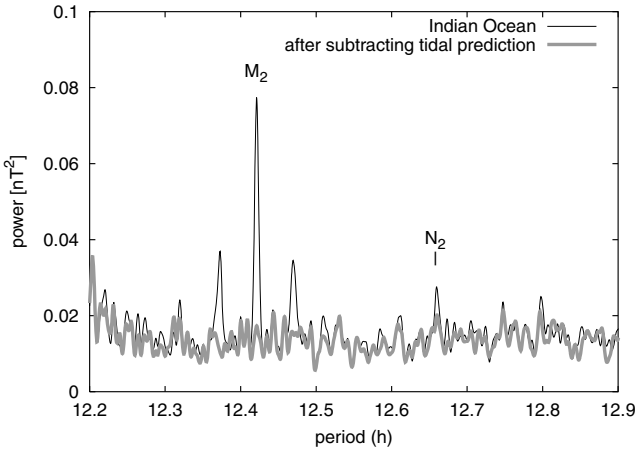

Figure 2. The spectrum of the magnetic residuals over the Indian Ocean shows clear peaks at the period of M2 (lunar tide) and a smaller at N2 (displaced by the lunar orbital frequency). Side lobes of M2 are an indication of the modulation by the semi-diurnal solar tide, S2. The observed frequency shift is due to the precession of the CHAMP orbit covering all local times within 130 days. After subtracting the predicted tidal signals, all of the spectral peaks disappear.

2.3 Division into high and low latitudes

High and low latitudes exhibit very different properties in terms of ionospheric current intensities. By low latitudes we mean here the range from -65° to 65° magnetic latitude. Ionization at low latitudes in the E-layer is caused almost exclusively by solar irradiation, while precipitation of energetic electrons and ions make a substantial contribution to ionization in the high-latitude regions at all times. Therefore, ionospheric currents largely vanish during night time at low latitudes while they remain active in the high-latitude regions even during complete darkness. A fortunate coincidence, on the other hand, is that the data coverage is thinnest at the quiet low latitudes and densest close to the noisy poles. In view of these differences we divide the data into overlapping high- and low-latitude segments and process these in different ways.

2.3.1 Vector data at low latitudes

Recognizing that most of the low-latitude noise is due to unmodelled contributions from magnetospheric currents, in particular the ring current (Maus *et al.* 2002), we fit and subtract a ring current field correction on a track-by-track basis. This correction includes only degree-1 fields, which results in three external and three induced field parameters. Of course, one would obtain much cleaner data by also including higher-degree internal and external field terms in the track-by-track filtering. However, this would lead to the removal of genuine lithospheric signal, which is to be avoided. Two additional coefficients were included, representing the far-field effect of northern and southern PEJs. These coefficients are described below. In addition, we solve for a set of angles accounting for a star camera misalignment with respect to the vector magnetometer, since this is a known problem of the CHAMP satellite. For every track we thus fit and subtract an 11-parameter model consisting of the three coefficients of an external dipole, three of an internal dipole, two polar electrojet strengths and three misalignment angles of an Euler rotation. Data were selected for quiet periods with Kp $\leq$ 2 from the local time sector 0:00–5:00 LT. The post-sunset equatorial ionosphere, however, is susceptible to local plasma instabilities forming so called plasma bubbles, which cause systematically positive magnetic deflections of up to 5 nT in the field strength. Contaminated tracks are identified by an automatic detection process and have been discarded. Herein, the field magnitude of the single tracks is high-pass filtered with a cut-off period of 30 s and is rectified. The filtered tracks are checked for peaks higher than 0.25 nT. Plasma instabilities are identified if also neighbouring peaks within a 6° latitudinal window are found. Coinciding with plasma bubbles we observe also a depletion in electron density. The occurrence rate of contaminated tracks varies from 0–80 per cent depending on longitude and season. A more detailed description of the detection process and the climatology of magnetic signatures due to bubble activity are given in Stolle *et al.* (2005).

2.3.2 Scalar data at low latitudes

Scalar data are not sensitive to the components of the external magnetic field, which are perpendicular to the main field. The main field resembles approximately that of an axial dipole and the CHAMP orbital plane is closely aligned with the magnetic meridian. Therefore, only two of the three components of an external dipole can be resolved by scalar data: one parallel to the main field dipole and one perpendicular, lying within the orbital plane. Two corresponding induced internal dipole coefficients can be defined. However, since

the external perpendicular dipole component turns out to be rather small, its induced counterpart should be even smaller. We have, therefore, omitted it in the cleaning procedure. We again include two coefficients representing the northern and southern PEJ fields. Attitude uncertainty is not an issue for scalar data. Data were selected from periods satisfying Kp $\leq$ 2 and 0:00–5:00 LT. Furthermore, we discard all tracks, which were identified as being contaminated by magnetic signals due to plasma instabilities in the ionospheric F-region (Stolle *et al.* 2005). After cleaning the data track by track, approximately 30 per cent of the tracks were discarded based on their rms signal strength relative to neighbouring tracks.

2.3.3 Scalar data at high latitudes

The same three-parameter ring current model was estimated track-by-track to correct the polar tracks. Following a study of the characteristics of ionospheric currents at high latitudes during very quiet periods (Ritter *et al.* 2004b), we selected data for interplanetary magnetic field (IMF) conditions $|\text{IMF } B_y| < 8$ nT and -2 nT $<$ IMF $B_z <$ 6 nT. Subsequently, the tracks with the lowest rms signal were used. For this selection, the polar tracks were ordered according to the longitude of the previous equator crossing. Then, all tracks that had at least one neighbouring track with significantly (difference $>$0.5 nT) smaller rms were rejected. About 95 per cent of the polar tracks were rejected by the IMF and rms criteria.

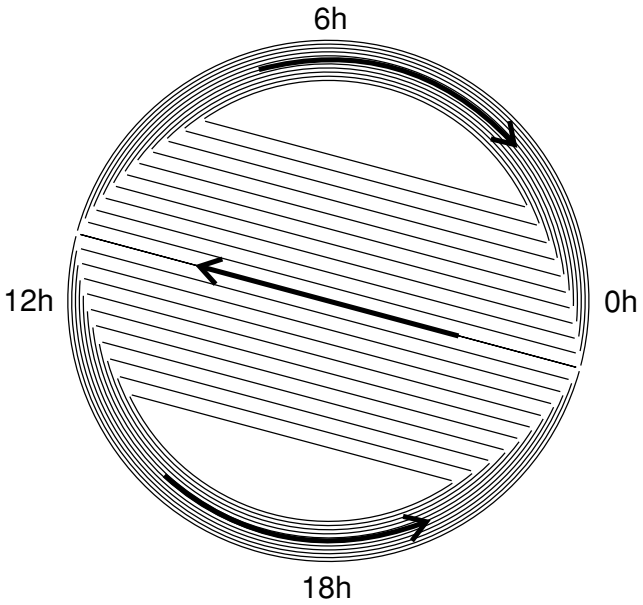

Figure 3. Our simple model of the PEJ system consists of 11 current arcs on the evening and 11 arcs on the morning sides. The currents are closed over the polar cap. The axis of symmetry is the 11/23 LT line, consistent with observations (Wang *et al.* 2005). To account for induction, the system is mirrored at a depth of 100 km below the surface, with the same current strength, but opposite direction.

2.4 Polar electrojet correction

Even during magnetically quiet periods PEJs have signal strengths of the order of 50 nT at 400 km altitude. The main current axis is located on average at about $\pm 70^\circ$ magnetic latitude. Unfortunately, an appreciable part of the related magnetic fields can be sensed quite far down to low latitudes. This far field effect cannot be considered as random noise because the PEJs are preferably directed from the day to the night side. Hence, during the LT interval of 0:00–5:00 used here, they flow westwards and generate a reduction in the ambient field magnitude at low latitudes, in the northern as well as the southern hemisphere. The main objective of the procedure described below is to remove this bias in order to avoid spurious negative anomalies at about 50°–65° north and south magnetic latitudes.

For the removal of this PEJ signal from the low-latitude data, we use the following approach. We use the data from half an orbit, ranging (almost) from pole to pole. A simple model current circuit represents the PEJs, sketched in Fig. 3. It consists of two systems of 11 closely spaced electrojet arcs with the current closure over the polar cap, one on the evening and one on the morning side. To account for induction effects, the system is mirrored by an equivalent current system flowing in the opposite direction, 200 km below the ionosphere. The assumption of a conductosphere below a depth of 100 km is in line with the results published by Mareschal (1976). The magnetic signal of the current system is evaluated numerically, by dividing the lines into 100 km segments and summing the magnetic effect (using Biot-Savart's law) of all segments. The model has only two free parameters: a scaling factor for the strength of the current and the diameter of the current arcs. We independently fit one such current system in the south and one in the north, each with two free parameters.

Since the polar current systems are not well represented in a global magnetic dipole coordinate system, we use separate coordinates for the northern and southern hemispheres, whose North and South poles correspond to the actual northern and southern dip poles. In the future, we plan to implement this model in corrected magnetic coordinates.

The magnetic signal is linearly dependent on the total current strength. On the other hand, the dependence on the arc-diameter is non-linear. Thus, fitting both parameters is a non-linear problem. A typical example is given in Fig. 4, upper frame. Due to the true complexity of the PEJ fields, even a rather good fit at high latitudes may still not remove the low-latitude effect sufficiently well. Therefore, in a second step, we retain the diameters of the southern and northern PEJ current arcs (removing the non-linearity of the problem) and fit the two southern and northern current amplitudes for the magnetic latitude range of -65° to 65° simultaneously with the magnetospheric ring current parameters (and star camera misalignment parameters for vector data) as described above. The result is shown in Fig. 4, lower frame. Fig. 5 shows the effect of the correction for the tracks within a 1° longitude interval of the southwestern Pacific Ocean. All tracks show the same lithospheric anomalies, but have varying magnetospheric and ionospheric contaminations. These are removed to a considerable extent with this correction. The PEJ correction is only applied to the low-latitude scalar and vector data. In order to avoid obscuring genuine lithospheric anomalies, this correction was designed in such a way that the latitudes of the PEJ source currents are always located outside of the region covered by the low-latitude track segment being considered. This is a reasonable assumption since the electrojets retreat polewards during quiet periods. A simplified version of this PEJ correction was already used in the MF3 model.

No special effort was made to remove induction effects from the Sq current system on the night side. Since this is primarily a large-scale effect, its signature is expected to be largely removed by the along-track filtering.

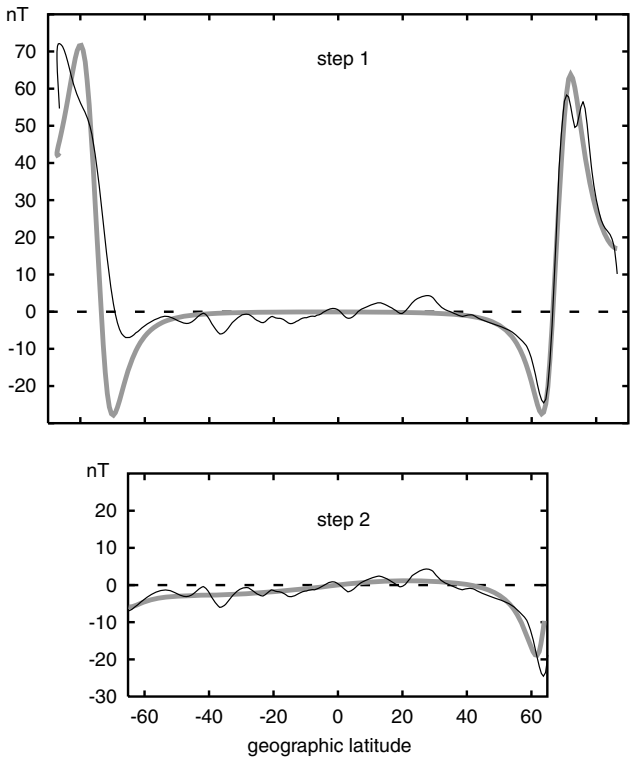

Figure 4. Removal of the far field of PEJs from low-latitude scalar data. First, the loop diameters and coarse current strengths of the northern and southern PEJs are found in a non-linear inversion (step 1). Subsequently, the loop diameters are held fixed and only the PEJ current strengths are estimated simultaneously with the three ring current parameters (six ring current plus three star camera parameters in case of vector data) from the data in the truncated -65° to 65° magnetic latitude range (step 2). For both steps, the best-fitting model is displayed here in grey and the observed scalar anomaly in black. In this particular example geographic and magnetic latitudes nearly coincide.

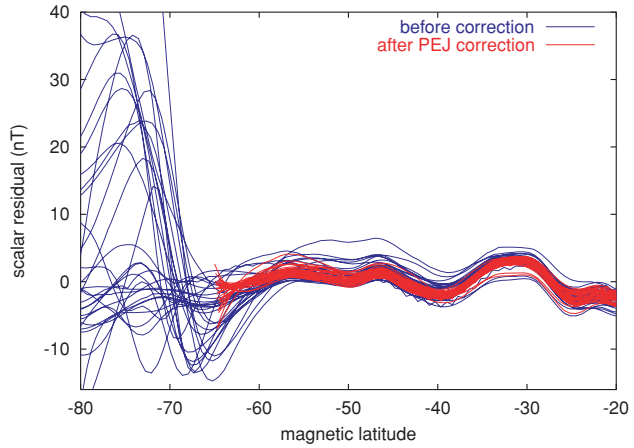

Figure 5. A typical selection of field residuals (blue) in a narrow longitude interval showing a clear minimum at -65° latitude. After the PEJ correction (red), the bias is removed and the scatter is reduced.

2.5 Line levelling

Despite the various measures to isolate the lithospheric signal by data selection, subtraction of models for the various contributions and filtering, significant unmodelled signal remains in the data. In particular, this noise leads to arbitrary offsets between adjacent satellite tracks. In aeromagnetic surveys, this well-known problem is dealt with by flying perpendicular tie lines and then adjusting the main flight lines in such a way as to minimize the misfits at the crossovers with the tie lines. This is called line levelling. For satellite data there are no tie lines, but one can nevertheless minimize the offsets between neighbouring tracks. Also, there are, in fact, crossover points between ascending and descending tracks.

Our line-levelling algorithm minimizes the distance-weighted misfit between all nearest pairs of measurements for all pairs of tracks. The weight function $W(\mathbf{r}_1, \mathbf{r}_2)$ is

$$W(\mathbf{r}_1, \mathbf{r}_2) = 1 - \frac{1}{R_s}\sqrt{(R_{\rm sat}\delta)^2 + 2(r_1 - r_2)^2}, \tag{1}$$

where $R_s = 800$ km is the search radius, $R_{\rm sat} = 6770$ km is the average orbital radius, and δ is the angular distance between the two locations $\mathbf{r}_1$ and $\mathbf{r}_2$. In this definition of the weight function, the altitude distance is upweighted by a factor 2 in order to account for the greater variability of the field in the vertical than in the horizontal direction.

We adjust the level of each track by subtracting a baseline correction corresponding to a degree-1 internal and degree-3 external field. The baseline correction parameters for the scalar data tracks at low and high latitudes are first computed in a single least-squares inversion minimizing the differences between all pairs of tracks. Then, the correction parameters for the vector data tracks are computed in a second inversion in which the offsets between these tracks, as well as the scalar offsets to the scalar data tracks, are minimized. As an example for the effect of the line levelling, the pre- and post-line-levelling scalar data are displayed for the Antarctic region in Fig. 6.

2.6 Least-squares estimation of Gauss coefficients

The SH coefficients of the scalar potential representing the lithospheric magnetic field are estimated to degree and order 90 using a standard least-squares approach. The magnetic potential of the lithospheric field can be represented as

$$V(r, \vartheta, \varphi, t) = R\sum_{\ell=1}^{N}\left(\frac{R}{r}\right)^{\ell+1}\sum_{m=-\ell}^{\ell} g_\ell^m \check{\beta}_\ell^m(\vartheta, \varphi), \tag{2}$$

where r, ϑ and φ are the radius, co-latitude and longitude, respectively, $R = 6371.2$ km is the traditional geomagnetic reference radius, N is the degree of the expansion, g_ℓ^m are the SH coefficients of the lithospheric field and $\check{\beta}_\ell^m(\vartheta, \varphi)$ are Schmidt semi-normalized surface SH functions in the convenient notation of Backus *et al.* (1996, p. 141)

$$\check{\beta}_\ell^m = \cos m\phi\ \check{P}_\ell^m(\cos\theta), \quad 0 \le m \le \ell, \tag{3}$$

$$\check{\beta}_\ell^{-m} = \sin m\phi\ \check{P}_\ell^m(\cos\theta), \quad 1 \le m \le \ell. \tag{4}$$

Here, the functions $\check{P}_\ell^m(\mu)$ are defined as

$$\check{P}_\ell^m(\mu) = \begin{cases} \sqrt{2\frac{(\ell-m)!}{(\ell+m)!}}P_\ell^m(\mu) & \text{if } 1 \le m \le \ell, \\ P_\ell(\mu) & \text{if } m = 0, \end{cases} \tag{5}$$

where $P_\ell^m(\mu)$ are the associated Legendre functions (Backus *et al.* 1996, eq. 3.7.2).

The coefficients g_ℓ^m, are estimated by finding the least-squares solution to the linear equation

$$\underline{G}\mathbf{m} = \mathbf{d}, \tag{6}$$

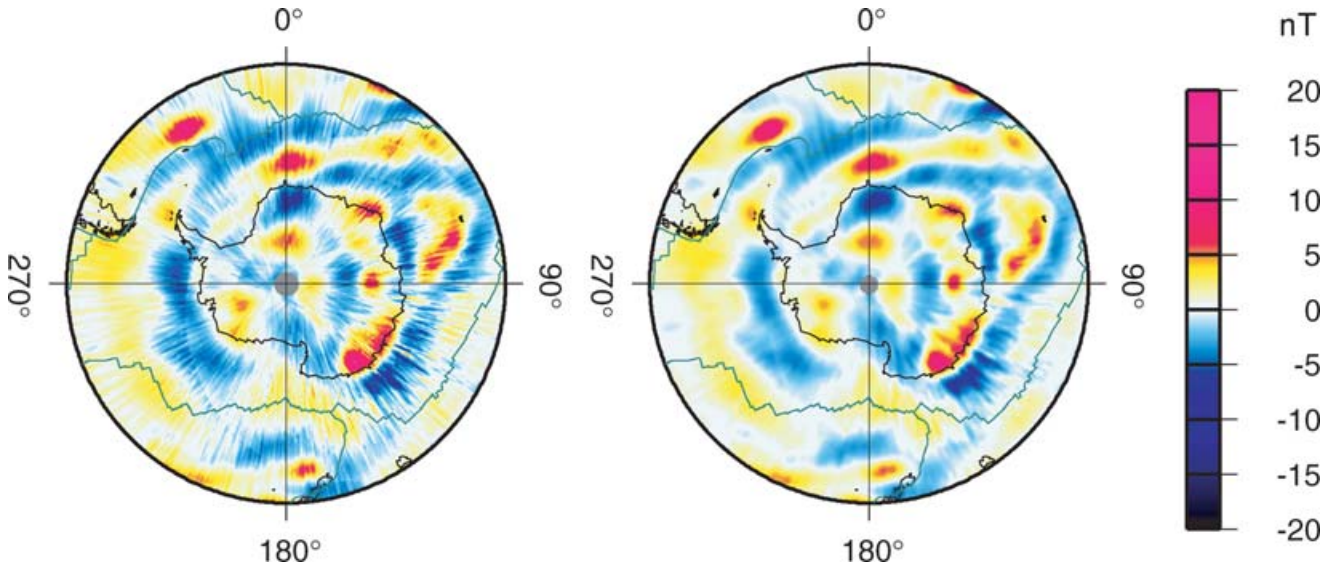

Figure 6. Scalar magnetic data before and after line levelling for the Antarctic region. The line levelling effectively removes offsets between neighbouring tracks. Two faint circular signatures indicate the overlap region of the low- and high-latitude tracks. The effect of the overlap is minimized in the final model estimation by rolling off the weights of the high-latitude tracks towards low latitudes and vice versa.

where **m** is the model vector, **d** is the data vector, and $\underline{\mathrm{G}}$ is Green's matrix, relating a unit perturbation in the model vector $\delta\mathbf{m}$ to the respective effect on the data vector $\delta\mathbf{d}$. Assuming that the small lithospheric field does not change the direction of the ambient magnetic field vector, $\underline{\mathrm{G}}$ is independent of **m**, even for scalar data.

The data are weighted in such a way as to give equal cumulative weight to every unit area $\delta\vartheta\delta\varphi\,\sin\vartheta$ on the sphere, by counting data numbers in equal area bins and downweighting them by the number density. We also tested the effect of weighting by including a diagonal covariance matrix with the local data standard deviations. However, this counteracts the area weighting and does not improve the solution. The least-squares solution to eq. (6) is

$$\mathbf{m} = (\underline{\mathrm{G}}^T\underline{\mathrm{G}})^{-1}\underline{\mathrm{G}}^T\mathbf{d}, \tag{7}$$

where the most time-consuming task is the computation of the normal equations matrix $\underline{\mathrm{G}}^T\underline{\mathrm{G}}$.

2.7 Regularization

In the least-squares estimation, the coefficients up to degree 60 are well determined, while certain higher-degree coefficients tend to 'blow up'. Such behaviour can have two reasons: either the coefficients are not well resolved by the spatial distribution of the data, or noise selectively contaminates certain coefficients. Examples for the first effect are the undetermined near-zonal coefficients when data with a large polar gap are used (e.g. Ørsted), or the $|m| = n$ coefficients, which are unresolved when only scalar data are used, known as the Backus effect (Backus 1970). However, CHAMP has a small polar gap and we are including vector data. Therefore, the problem is obviously caused by noise, rather than a lack of resolution. The source of this noise is found in random offsets between adjacent tracks, which cause certain coefficients to 'blow up'. This behaviour is illustrated by plotting the deviation of the coefficient power from a crude power model, as shown in Fig. 7(a). Here, the

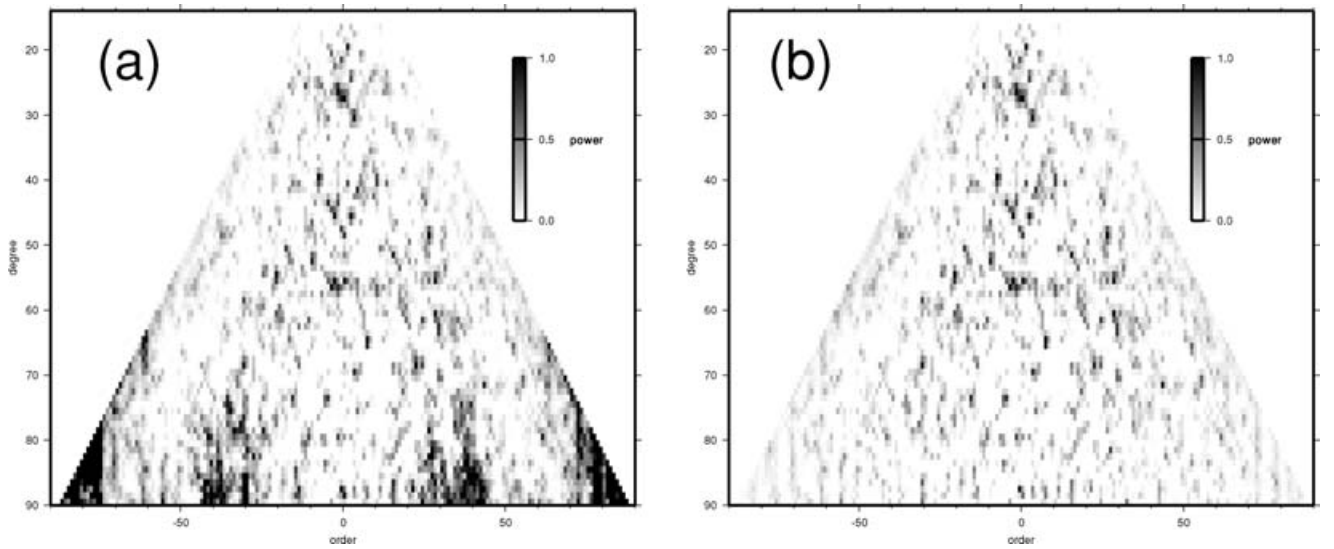

Figure 7. Deviation of the Gauss coefficient power from the expectation given by eq. (9) before (a) and after (b) the regularization. Only coefficients above degree 60 are regularized. Displayed here are the eight-point averages of these power deviations (GMT command *nearneighbor -N8*, (Wessel & Smith 1991)).

power of an individual SH coefficient is defined as

$$R_\ell^m = (\ell+1)\left(g_\ell^m\right)^2, \tag{8}$$

and our empirical power model is given by

$$R_0(\ell, m) = 0.1 + 0.35(1 - m/\ell)^2. \tag{9}$$

Above degree 60 there are groups of coefficients, which are contaminated by noise, resulting in systematically increased power. Such clusters of coefficients with increased power were damped by the following scheme: For each $\ell > 60$ and each order m, we compute the distance-weighted mean power

$$\overline{R}(\ell, m) = \frac{1}{R_{\rm W}} \sum_{i=-5}^{5} \sum_{k=-3}^{3} \left(1 - \sqrt{\frac{i^2+k^2}{5^2+3^2}}\right) (\ell+1+i)\left(g_{\ell+i}^{m+k}\right)^2, \tag{10}$$

in the Gauss coefficients space for a 11×7 element rectangle centred around the considered coefficient ℓ, m, where index pairs with $|m+k| > |\ell+i|$ are omitted. Here, $R_{\rm W}$ is the sum of the weights in the large, round brackets. In case $\overline{R}(\ell, m)$ exceeds the empirical power model (eq. 9) by more than 10 per cent, the coefficient is damped (regularized) by multiplying the corresponding diagonal element in the $\underline{\mathrm{G}}^T\underline{\mathrm{G}}$-matrix with $\sqrt{\overline{R}(\ell, m)/R_0(\ell, m)}$, which brings its power down to the expected level. The resulting MF4 coefficient matrix is shown in Fig. 7(b). The corresponding field that has been suppressed in the regularization is displayed in Fig. 8. It reveals line-levelling issues as the main sources of noise in the data. At low latitudes, these are caused primarily by unmodelled F-region ionospheric currents, while at high latitudes the noisy regions are concentrated in the polar electrojet regions. Differing PEJ strengths between adjacent satellite tracks lead to arbitrary offsets between tracks, seen here as across-track noise.

Due to errors in the main field model and other contaminations, the coefficients for SH degrees 1–15, which are co-estimated, are not zero. However, their power is more than one order of magnitude

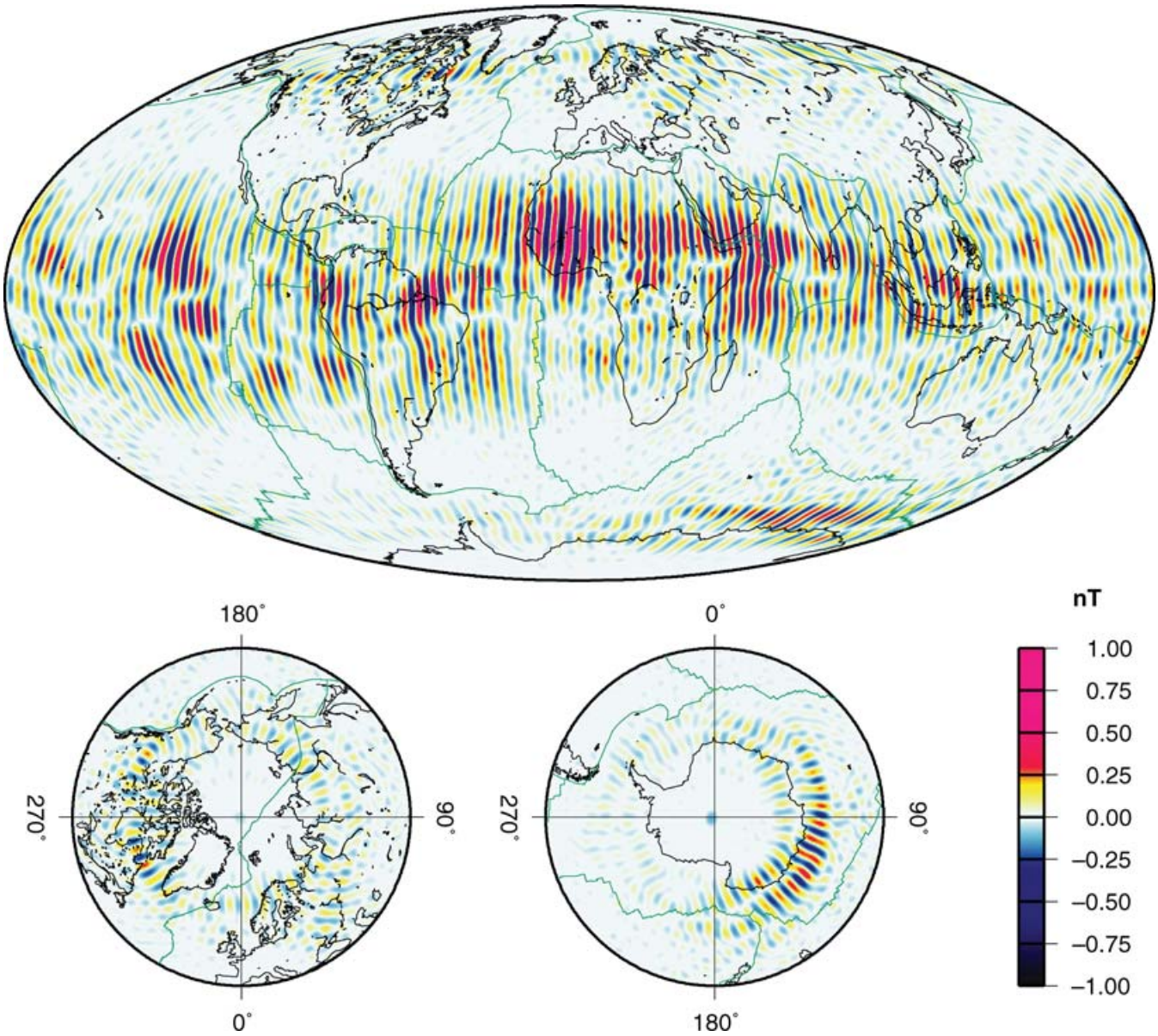

Figure 8. Map of the difference between the unregularized and the finally regularized MF4 model, displayed is the B_z component at 400 km altitude. The meridional stripes are clearly due to line-levelling problems.

lower than the lithospheric field power and these coefficients are set to zero for the final MF4 model.

3 RESULTS AND DISCUSSION

In this section, we present the resulting MF4 model in view of the intended applications 1–3 (see Introduction), and provide an outlook on future revisions of the model.

3.1 Misfit between the model and input data

In field modelling, one often looks at the rms misfit between the model and the input data. Figs 9(a) and (b) show maps of mean rms residuals of the scalar and vector data against the final MF4 model. In order to make the two kinds of data comparable, the vector residuals were defined as

$$rms_{\mathrm{vec}} = \sqrt{\frac{1}{3n}\sum_{i=1}^{n}\left|\mathbf{B}^{i}_{\mathrm{observed}} - \mathbf{B}_{\mathrm{model}}\right|^{2}}, \tag{11}$$

where n is the number of observations in the considered area, and we divide by $3n$ to obtain a per-component rms, which is directly comparable with the rms of the scalar residuals.

As expected, residuals in the polar regions are larger than at lower latitudes, although it is presently not clear why the residuals in the northern are larger than in the southern polar region. Interestingly, the residuals for the vector components are not larger than those of the scalar data. This is an indication of the low attitude-noise in the CHAMP data, after a constant attitude bias has been removed. Furthermore, the low vector-component residuals mean that field-aligned currents, which are only visible in the vector data, do not make a significant contribution to the low-latitude magnetic field at 0:00–5:00 LT. In the residuals of the previous MF3 model, there was a band of disturbances aligned with the dip equator, caused by local plasma instabilities (Lühr *et al.* 2002). Having rejected tracks disturbed by F-region currents (Stolle *et al.* 2005), this band is no longer visible. In general, one should be aware that systematic errors may exceed the values indicated by these residual maps. The main sources of systematic error are the removal of genuine lithospheric signal in the track by track filtering and distortions caused by unmodelled fields. The latter include errors in the main field model, secular variation and secular acceleration, ocean currents (Tyler *et al.* 2003), electromagnetic induction effects (Kuvshinov *et al.* 2002) and the diamagnetic effect of high-density plasma regions through which CHAMP is flying (Lühr *et al.* 2003).

3.2 Views of the Model at 400 km and 50 km altitude

The vertical component of the lithospheric magnetic field at a satellite altitude of 400 km is shown in Fig. 10. The strongest anomalies on the continents are associated with Proterozoic provinces, which are often covered by Phanerozoic sediments. In the oceans, strong anomalies are caused by units which were formed on continental margins during the break-up of Gondwana [e.g. Maud (MD) and Agulhas Plateau (AG)]. The symbol in parentheses is shown in Figs 10 and 11. Large sections of oceanic crust have acquired a normal remanent magnetization during the Cretaceous superchron. Associated remanent anomalies are visible, for example, on both sides of the Atlantic Mid-Ocean Ridge, as well as between Australia and Antarctica.

There is significant improvement of the lithospheric anomaly features in the MF4 model compared to the earlier MF1 model (Maus *et al.* 2002). Over the continents, anomalies have sharpened along the Tornquist–Teisseyre Zone (TTZ) over the East European craton and over the shield regions of Guyana (GY), South America. The anomalies over the Kentucky–Tennessee (KT) region, central USA, which appeared as a single bell-shaped anomaly in MF1 now appears as two separate anomalies. Major anomaly features over the Cathaysian-Indian plate, like the Sichuan Massif (SM) and the anomaly along Central Pakistan (CP), have increased in amplitude.

In view of the intended applications 2 and 3 it is often useful to display the model closer to the Earth's surface. However, this enhances not only the genuine lithospheric features but also amplifies model errors, in particular at the short wavelengths. At low latitudes, 50 km is the lowest altitude recommended for MF4. As expected, the model is much less reliable in the polar regions where even a map at 100 km altitude appears noisy. However, noise levels have dropped significantly over the Antarctic from MF3 to MF4. It is not clear at the moment why the arctic is particularly difficult to map. Fig. 11 shows the lithospheric anomalies for two selected areas at an altitude of 50 km above the surface. Numerous interesting geological features are visible, many of which have been discussed in the literature, summarized by Langel & Hinze (1998). For instance, the mid-Proterozoic province of the Kentucky–Tennessee region now appears as a conglomeration of anomalies of smaller extent. Over the oceans, subduction zones—notably, the Middle America (MA) Trench along the southwestern coast of Mexico, further north along the edge of Canadian Cordillera, the Cascades (CS) and the Aleutians (AL) along southern Alaska, the Kurile–Kamchatka (KK) Trench (stretching from north of Japan to Kamchatka Peninsula), the Ryukyu (RY) Trench, extending from south of Japan to the Philippines and the Izu–Bonin–Mariana (IM) Trench located south of Japan—are delineated remarkably well. Another stretch of subduction zones are also evident along the New Britain–Solomon (BS) Arc that stretches up to the Vanuatu–Tonga (VT) Arc north and east of New Guinea. Subduction zone anomalies are also evident over the Java Trench (JT), Indonesia, over the Scotia (SS) Arc, in the South Atlantic Ocean, over the Lesser Antilles (LA) in the central Atlantic Ocean, and the Aeolian–Aegean (AA) Arc south of Italy and Greece, the latter being only weakly visible at satellite altitude (*cf.* Fig. 10). There are other subduction zones which are poorly resolved, such as along the western coast of the South American (SA) continent, stretching down to South Shetlands, along the Philippine (PL) Islands, the Tonga–Kermadec Trench (TK) located northeast of New Zealand and the Macquarie (MQ) Arc extending southeast from south of New Zealand. All subduction zones are shown as thick light green lines in Figs 10 and 11 against the thinner dark green lines that mark the plate boundaries. Over the continental regions, the most prominent subduction zones visible are over the Himalayas (HM). Subduction zones along the Zagros (ZG) and the Alps (AP) mountains are not evident, though. Modelling these anomalies yields new insights into the structure and dynamics of the crust (Purucker & Ishihara 2005). A particularly interesting example is the subduction zone along the western coast of Sumatra, Indonesia, which is clearly visible in MF4 and MF3, but was not visible in the Magsat maps (Langel & Hinze 1998, pp. 202–207).

3.3 Outlook

While the MF models are becoming increasingly accurate at lower latitudes, progress in the polar regions is so far mainly based on the steadily increasing data volume. Our present strategy is to select for favourable IMF conditions (Ritter *et al.* 2004b; Olsen 2002)

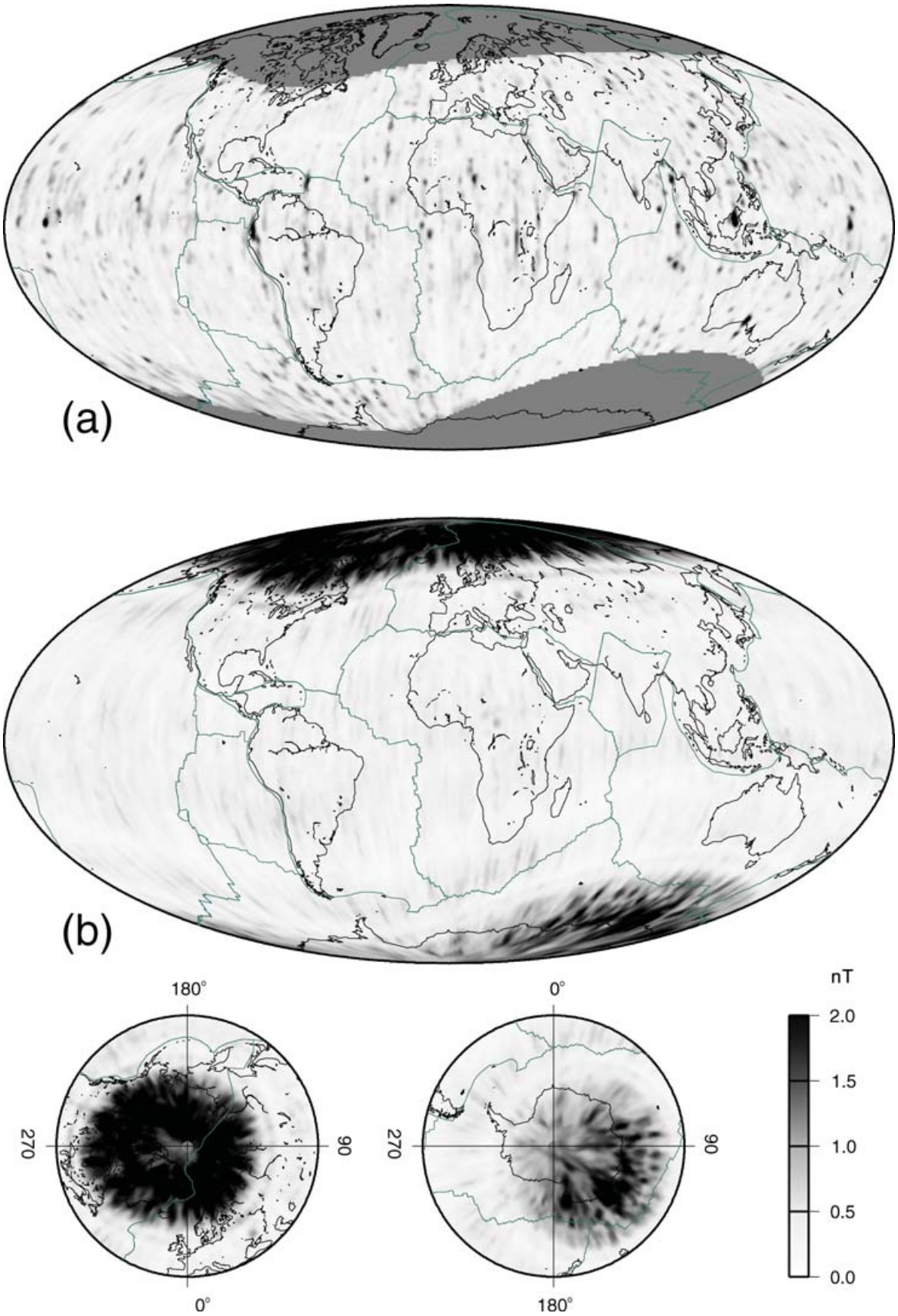

Figure 9. The rms of vector component (a) and scalar (b) residuals of the cleaned input data against the final MF4 model.

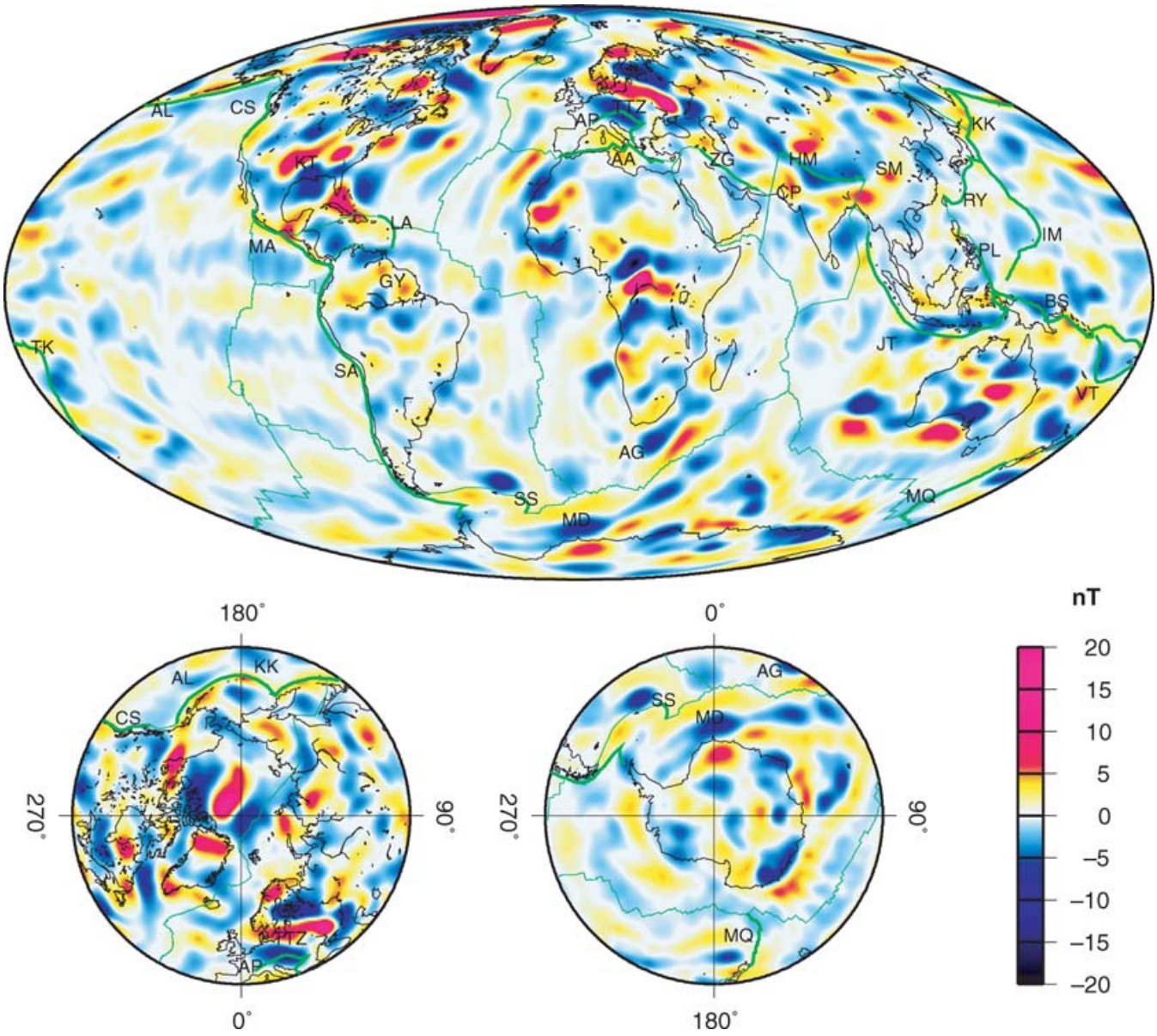

Figure 10. Vertical component of the lithospheric magnetic field at a satellite altitude of 400 km above the mean Earth radius, as given by MF4. Plate boundaries are indicated as thin, dark green lines, subduction zones as thick, light green lines.

and then identify the quietest tracks by their absolute rms strength. This assumes that the remaining ionospheric contributions make a positive contribution to the rms, which may not always be correct. A possibility to be investigated is to fit and subtract a PEJ model, possibly constrained by independent observatory and satellite data.

Future significant improvements can be expected in the MF model series from CHAMP due to

(1) the steadily decreasing altitude of the spacecraft,
(2) corrections for the diamagnetic effect using electron temperature and density measurements of the Langmuir probe and
(3) better models of electromagnetic induction in the ocean, crust and mantle.

Finally, an important next step will be the combined modelling of satellite measurements with near-surface marine and aeromagnetic compilations, which could significantly improve the accuracy of the global models at the Earth's surface.

4 MODEL AVAILABILITY

The MF4 SH coefficients, images and animations of the lithospheric field at different altitudes, grids of the vertical component, the total intensity, its spatial derivatives and the analytic signal (Ravat *et al.* 2002a) are available on the MF4 web site at http://www.gfz-potsdam.de/pb2/pb23/SatMag/litmod4.html.

ACKNOWLEDGMENTS

Figs 7, 8, 9, 10 and 11 were displayed using GMT (Wessel & Smith 1991). This work is supported by the Deutsche Forschungsgemeinschaft as part of the Special Programme 'Geomagnetic Variations' (SPP 1097). The operational support of the CHAMP mission by the German Aerospace Center (DLR) and the financial support for the data processing by Federal Ministry of Education and Research (BMBF) are gratefully acknowledged.

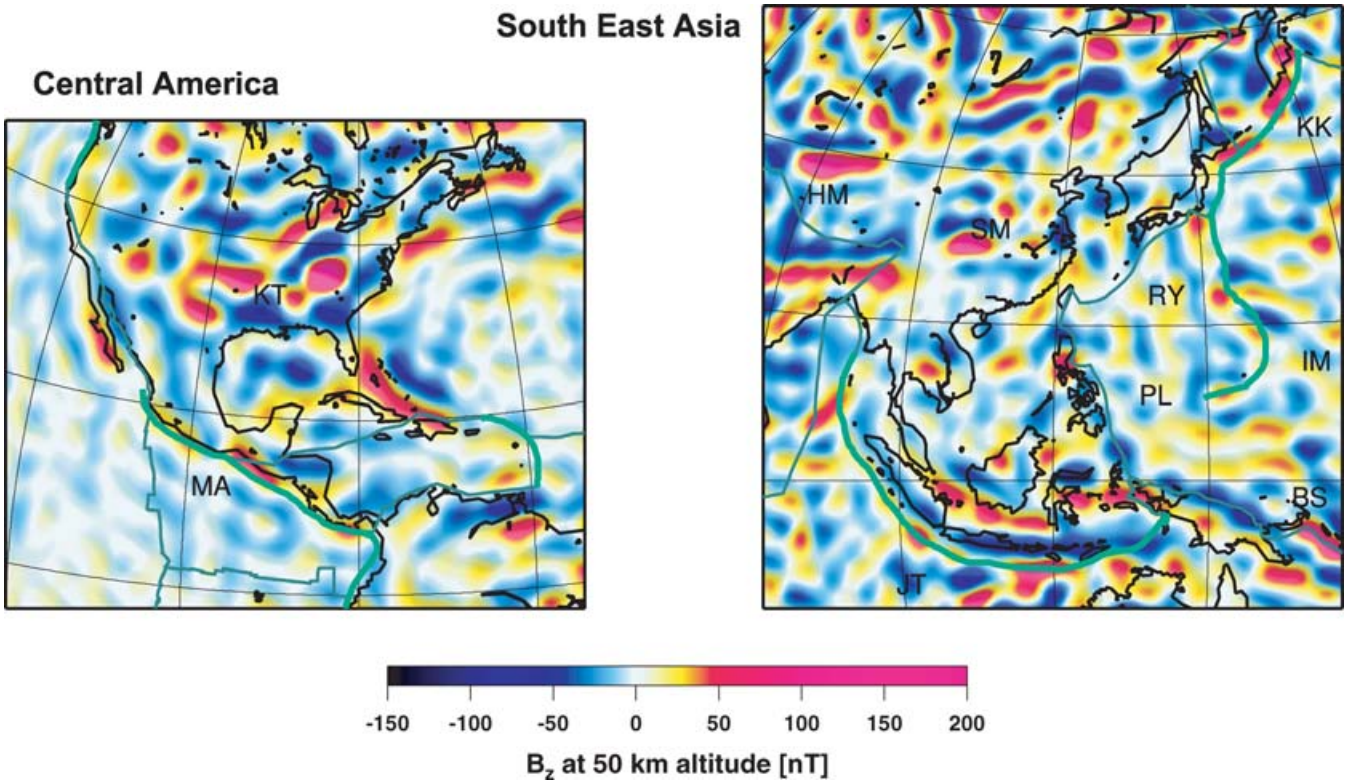

Figure 11. Vertical component of the lithospheric magnetic field downwards continued to an altitude of 50 km above the surface for two areas with strong lithospheric magnetic anomalies. Plate boundaries are indicated as thin, dark green lines, subduction zones as thick, light green lines.

REFERENCES

Achache, J., Abtout, A. & LeMouel, J., 1987. The downward continuation of Magsat crustal anomaly field over southeast Asia, *J. geophys. Res.,* **92,** 11 584–11 596.

Arkani-Hamed, J., Langel, R.A. & Purucker, M., 1994. Scalar magnetic anomaly maps of Earth derived from POGO and Magsat data, *J. geophys. Res.,* **99,** 24 075–24 090.

Backus, G., Parker, R.L. & Constable, C., 1996. *Foundations of Geomagnetism*, Cambridge University Press, Cambridge.

Backus, G.E., 1970. Non-uniqueness of the external geomagnetic field determined by surface intensity measurements, *J. geophys. Res.,* **75,** 6339–6341.

Cain, J.C. & Sweeney, R.E., 1973. The POGO data, *J. Atm. Terr. Phys.,* **35,** 1231–1247.

Cain, J.C., Wang, Z., Kluth, C. & Schmitz, D.R., 1989. Derivation of a geomagnetic model to n = 63, *Geophys. J. Int.,* **97,** 431–441.

Cohen, Y. & Achache, J., 1990. New global vector magnetic anomaly maps derived from Magsat data, *J. geophys. Res.,* **95,** 10 783–10 800.

Erofeeva, S. & Egbert, G., 2002. Efficient inverse modelling of barotropic ocean tides, *J. Atmosph. Ocean. Technol.,* **19,** 183–204.

Fox Maule, C., Purucker, M.E., Olsen, N. & Mosegaard, K., 2005. Heat flux anomalies in Antarctica revealed by satellite magnetic data, *Science,* **309,** 464–467, doi: 10.1126/science.1106888.

Hemant, K., Maus, S. & Haak, V., 2005. Interpretation of CHAMP crustal field anomaly maps using a geographical information system (GIS) technique, in *Earth Observation with CHAMP: Results from Three Years in Orbit*, pp. 249–254, eds Reigber, C., Lühr, H., Schwintzer, P. & Wickert, J., Springer, Berlin, Heidelberg.

Kuvshinov, A. & Olsen, N., 2005. 3-D Modelling of the Magnetic Field Due to Ocean Tidal Flow, in *Earth Observation with CHAMP: Results from Three Years in Orbit*, pp. 359–365, eds Reigber, C., Lühr, H., Schwintzer, P. & Wickert, J., Springer, Berlin, Heidelberg.

Kuvshinov, A.V., Olsen, N., Avdeev, M.B. & Pankratov, O.V., 2002. Electromagnetic induction in the oceans and the anomalous behaviour of coastal C-responses for periods up to 20, *Geophys. Res. Lett.,* **29,** doi: 10.1029/2001GL014,409.

Langel, R.A. & Hinze, W.J., 1998. *The Magnetic Field of the Earth's Lithosphere—the Satellite Perspective*, Cambridge University Press, Cambridge.

Laske, G. & Masters, G., 1997. A global digital map of sediment thickness, *EOS, Trans. Am. geophys. Un.,* **78,** F483.

Lühr, H., Maus, S., Rother, M. & Cooke, D., 2002. First in situ observation of night time F region currents with the CHAMP satellite, *Geophys. Res. Lett.,* **29,** doi: 10.1029/2001GL013,845.

Lühr, H., Rother, M., Maus, S., Mai, W. & Cooke, D., 2003. The diamagnetic effect of the equatorial Appleton anomaly: its characteristics and impact on geomagnetic field modeling, *Geophys. Res. Lett.,* **30**(17), doi: 10.1029/2003GL017,407.

Mareschal, M., 1976. On the problem of simulating the Earth's induction effect in modelling polar magnetic substorms, *Rev. Geophys. Space Phys.,* **14,** 403–409.

Maus, S. & Lühr, H., 2005. Signature of the quiet-time magnetospheric magnetic field and its electromagnetic induction in the rotating Earth, *Geophys. J. Int.,* doi: 10.1111/j.1365–246X.2005.02691.x.

Maus, S., Rother, M., Holme, R., Lühr, H., Olsen, N. & Haak, V., 2002. First scalar magnetic anomaly map from CHAMP satellite data indicates weak lithospheric field, *Geophys. Res. Lett.,* **29**(14), doi: 10.1029/2001GL013,685.

Maus, S., Lühr, H., Balasis, G., Rother, M. & Mandea, M., 2005. Introducing POMME, Potsdam Magnetic Model of the Earth, in *Earth Observation with CHAMP: Results from Three Years in Orbit*, pp. 293–298, eds Reigber, C., Lühr, H., Schwintzer, P. & Wickert, J., Springer, Berlin, Heidelberg.

Olsen, N., 2002. A model of the geomagnetic main field and its secular variation for epoch 2000 estimated from Ørsted data, *Geophys. J. Int.,* **149,** 454–462.

Purucker, M.E. & Ishihara, T., 2005. Magnetic images of the Sumatra region crust, *EOS, Trans. Am. geophys. Un.,* **86**(10), doi: 10.1029/2005EO100,002.

Ravat, D., Langel, R.A., Purucker, M., Arkani-Hamed, J. & Alsdorf, D.E., 1995. Global vector and scalar Magsat magnetic anomaly maps, *J. geophys. Res.,* **100,** 20 111–20 136.

Ravat, D., Wang, B., Wildermuth, E. & Taylor, P., 2002a. Gradients in the interpretation of satellite-altitude magnetic data: and example from central africa, *Geodynamics,* **33,** 131–142.

Ravat, D., Whaler, K.A., Pilkington, M., Sabaka, T. & Purucker, M., 2002b. Compatibility of high-altitude aeromagnetic and satellite-altitude magnetic anomalies over Canada, *Geophysics,* **67,** 546–554.

Regan, R.D., Cain, J.C. & Davis, W.M., 1975. A global magnetic anomaly map, *J. geophys. Res.,* **80,** 794–802.

Reigber, C., Lühr, H. & Schwintzer, P., 2002. CHAMP mission status, *Adv. Space Res.,* **30,** 129–134.

Ritter, P., Lühr, H., Viljanen, A., Amm, O., Pulkkinen, A. & Sillanpaa, I., 2004a. Ionospheric currents estimated simultaneously from CHAMP satellite and IMAGE ground-based magnetic field measurements: a statistical study at auroral latitudes, *Ann. Geophys.,* **22,** 417–430.

Ritter, P., Lühr, H., Viljanen, A. & Maus, S., 2004b. High-latitude ionospheric currents during very quiet times: their characteristics and predictability, *Ann. Geophys.,* **22,** 2001–2014.

Sabaka, T.J., Olsen, N. & Purucker, M.E., 2004. Extending comprehensive models of the Earth's magnetic field with ørsted and CHAMP data, *Geophys. J. Int.,* **159,** 521–547.

Schmucker, U., 1985. Electrical properties of the Earth's interior, in *Landolt-Börnstein, New-Series, 5/2b*, pp. 370–397, Springer-Verlag, Berlin, Heidelberg.

Stolle, C., Lühr, H., Rother, M. & Balasis, G., 2005. Magnetic signatures of equatorial spread F, as observed by the CHAMP satellite, *J. geophys. Res.,* in press.

Sutcliffe, P.R. & Lühr, H., 2003. A comparison of Pi2 pulsations observed by CHAMP in low Earth orbit and on the ground at low latitude, *Geophys. Res. Lett.,* **30,** doi: 10.1029/2003GL018,270.

Tyler, R., Maus, S. & Lühr, H., 2003. Satellite observations of magnetic fields due to ocean tidal flow, *Science,* **299,** 239–241.

Wang, H., Lühr, H. & Ma, S.Y., 2005. Solar zenith angle and merging electric field control of field-aligned currents: A statistical study of the southern hemisphere, *J. geophys. Res.,* **110,** A3, A03306, doi:10.1029/2004JA010530.

Wessel, P. & Smith, W.H.F., 1991. Free software helps map and display data, *EOS, Trans. Am. geophys. Un.,* **72,** 441.